Journal of Energy Chemistry 72 (2022) 395–404

Contents lists available at ScienceDirect

Journal of Energy Chemistry

journal homepage: www.elsevier.com/locate/jechem

http://www.journals.elsevier.com/journal-of-energy-chemistry/

Delicate surface vacancies engineering of Ru doped MOF-derived Ni-NiO@C hollow microsphere superstructure to achieve outstanding hydrogen oxidation performance

Yuting Yang [a], Yi Huang [a], Shuqing Zhou [a], Yi Liu [a], Luyan Shi [a], Tayirjan Taylor Isimjan [b,*], Xiulin Yang [a,*]

[a] Guangxi Key Laboratory of Low Carbon Energy Materials, School of Chemistry and Pharmaceutical Sciences, Guangxi Normal University, Guilin 541004, Guangxi, China
[b] Saudi Arabia Basic Industries Corporation (SABIC) at King Abdullah University of Science and Technology (KAUST), Thuwal 23955-6900, Saudi Arabia

ARTICLE INFO

Article history:
Received 9 April 2022
Revised 2 June 2022
Accepted 7 June 2022
Available online 14 June 2022

Keywords:
Ru/Ni-NiO@C
Vacancy defects
Electrocatalysis
Metal-organic framework
Hydrogen oxidation

ABSTRACT

Surface vacancy defects, as the bridge between theoretical structural study and the design of heterogenous catalysts, have captured much attention. This work develops a metal-organic framework-engaged replacement-pyrolysis approach to obtain highly dispersed Ru nanoparticles immobilized on the vacancy-rich Ni-NiO@C hollow microsphere (Ru/Ni-NiO@C). Fine annealing at 400 °C introduces nickel and oxygen vacancies on Ru/Ni-NiO@C surface, resulting in an improved electrical conductivity and rapid mass-charge transfer efficiency. Ru/Ni-NiO@C with a hollow micro/nanostructure and interconnected meso-porosity favors the maximal exposure of abundant active sites and elevation of hydrogen oxidation reaction (HOR) activity. Experimental results and density functional theory (DFT) calculations reveal that an electronic effect between Ru and Ni-NiO@C, in conjunction with nickel/oxygen vacancies in the NiO species could synergistically optimize hydrogen binding energy (HBE) and hydroxide binding energy (OHBE). The HBE and OHBE optimizations thus created confer Ru/Ni-NiO@C with a mass activity over 7.75 times higher than commercial Pt/C. Our work may provide a constructive route to make a breakthrough in elevating the hydrogen electrocatalytic performance.

1. Introduction

Fuel cell technologies have stimulated substantial attention by virtue of their high energy density, high energy conversion efficiency, and environmental compatibility, which lay the foundation for the sustainable development of society [1]. Among several types of fuel cells, proton exchange membrane fuel cells (PEMFCs) and hydroxide exchange membrane fuel cells (HEMFCs) are the leading hydrogen utilization techniques at low temperature [2,3]. However, the commercialization of PEMFCs is inevitably plagued by expensive Pt-based catalysts and per-fluorinated membranes. HEMFCs give critical merits over PEMFCs due to the possibility of using non-precious metal-based catalysts, milder alkaline working conditions, and cheaper bipolar plates [3]. Unfortunately, the anode hydrogen oxidation reaction (HOR) activity on precious metals is approximately two orders of magnitude drop when switching from acidic to alkali electrolytes [4,5]. There are significant differences between the HOR in alkaline ($H_2 + 2OH^- \rightarrow 2H_2O + 2e^-$) and acidic ($H_2 \rightarrow 2H^+ + 2e^-$) media [6]. Accordingly, two descriptors of hydrogen binding energy (HBE) and hydroxide binding energy (OHBE) have been reported to verify the origin of slow alkaline HOR kinetics [4,7,8]. Following Sabatier's principle, the most active HOR electrocatalysts can be correlated with the calculated HBE on the metal surfaces via a volcano relationship [9]. This correlation suggests that HBE is used as a dominant descriptor for alkaline HOR activity. However, proton donor is changed from H_3O^+ in acidic to H_2O in alkaline conditions plus the existences of OH^- species, the Volmer step is the rate-determining step in alkaline HOR [10]. Thus, a bifunctional mechanism that balanced optimal HBE and OHBE/oxophilicity has been propounded to design the alkaline HOR electrocatalysts with better performance [6,8,10]. For example, Li et al. have done pioneering works on the fabrication of BCC-phased PdCu, which showed higher HOR activity owing to the synergistic interplay between HBE and OHBE [11]. Yu et al. also demonstrated that synergistic optimization of HBE and OHBE on $MoNi_4$ determined the HOR activity in alkali medium [8]. Furthermore, we reported HBE and OHBE played equally important roles for the enhancement of HOR activity [12,13].

* Corresponding authors.
E-mail addresses: isimjant@sabic.com (T.T. Isimjan), xlyang@gxnu.edu.cn (X. Yang).

https://doi.org/10.1016/j.jechem.2022.06.011

Ruthenium possesses the lower price and favorable Ru–H bond strength, and its HOR activity can be potentially increased to approaching that of Pt/C after fine-tuning [12,14]. Zhuang et al. showed that the HOR activity of Pt-based materials can be optimized by alloying with Ru, however, Ru shows low HOR activity. As Pt is the significant component of PtRu/C, it still has a high cost [15]. Replacing platinum metals with cheap catalysts is a critical step to tackling the inherent disadvantages of Pt-based catalysts. Ni-based materials have an emerging impact in this perspective, which are helpful for alkaline HOR, such as Ni/NiO/C [7], Ni/MoO_2 [16], and CeO_2/Ni [17], but their HOR activity and durability are still lagging far behind the benchmark Pt/C. Another plausible stratagem to enhance the HOR activity is the introduction of metal-support effect since it creates a strong metal-support interaction (SMSI), which

is performed until the Hellmann-Feynman force on each atom is smaller than 0.03 eV $Å^{-1}$. The energy criterion is set to 10^{-6} eV in iterative solution of the Kohn-Sham equation. The Kohn-Sham valence electronic wavefunction was expanded in a plane-wave basis set with a cutoff at 400 eV. Adsorption energy was calculated according to $E_{adsorption} = E_{total} - E_{substrate} - E_{adsorbate}$.

3. Results and discussion

3.1. Synthesis and structural characterization

Forming microspherical hollow structure in the precursor requires pertinent structure engineering. We bring up a MOF-engaged replacement-pyrolysis technique to achieve such goal. Fig. 1(a) schematically depicts the synthesis process of Ru/Ni-NiO@C hollow microsphere superstructure (see Experimental methods for more details). Firstly, $Ni(NO_3)_2{\cdot}6H_2O$ is used as the Ni precursor and trimesic acid is selected as the organic ligand. Polyvinylpyrrolidone (PVP) acts as a structure-directing agent to create defect-rich hollow spherical structure for the growth of MOF via a simple hydrothermal method. The Ni-MOF with accessible large interior cavities can accommodate foreign active metals well [28]. Subsequently, the Ru precursor, $RuCl_3$, may be confined to the inner and outer shells of the Ni-MOF hollow microspheres through the galvanic replacement reaction, forming a Ru/Ni-MOF hybrid structure. Finally, the thus-obtained Ru/Ni-MOF composite was heated in a tube furnace at 400 °C for 4 h under N_2 flow to activate the metal sites. The Ru^{3+} was converted to metallic Ru nanoparticles (NPs). Ni species in the carbonized MOF were converted into Ni-NiO@C heterojunction structure. The organic ligands were carburized to form partially graphitic support. The expected Ru content is 3.8 wt% confirmed by ICP-AES measurements. As displayed in Table S1, Ru contents vary from 2.9 wt% to 5.1 wt% for these samples, in which the sample with 3.8 wt% Ru was investigated in detail in this work (denoted as Ru/Ni-NiO@C in the main text). Ru/NiO@C (300 °C), Ru/Ni-NiO@C-500, and Ru/Ni-NiO@C-600 were prepared under a similar protocol except for the pyrolysis temperatures (300, 500, 600 °C, respectively). As reported in the literature, the morphology of MOFs-derived material is tightly correlated with the carbonization temperatures, which is further determined by the TGA. High-temperature (>600 °C) pyrolysis usually makes the MOFs skeleton prone to collapse. We then carried out a TGA to reveal the decomposition of organic linker dependence on carbonization temperatures. The thermal behavior of Ni-MOF under N_2 atmosphere is presented in Fig. 1(b), the weight loss of Ni-MOF up to 300 °C is mainly caused by the evaporation of absorbed water and DMF molecule. Subsequently, a significant mass loss in 300–400 °C is originated from both the decomposition of organic ligands and the transformation of Ni^{2+} to NiO. In the temperature range of 400–800 °C, the weight loss is corresponding to the reduction of NiO to metallic Ni by the carbon [20]. As evidenced by the TGA, we chose to carbonize MOFs at 400 °C. After annealing, the XRD (Fig. 1c) signals of NiO (JCPDS: 47-1049) can be detected at low temperature (300 °C). Moreover, the diffraction peaks at 44.5°, 51.8°, and 76.4° are indexed to the metallic Ni (JCPDS: 04-0850) at higher annealing temperatures (400–600 °C) [20]. No diffraction peaks being ascribable to Ru can be discernible, indicating that Ru in Ru/Ni-NiO@C is amorphous

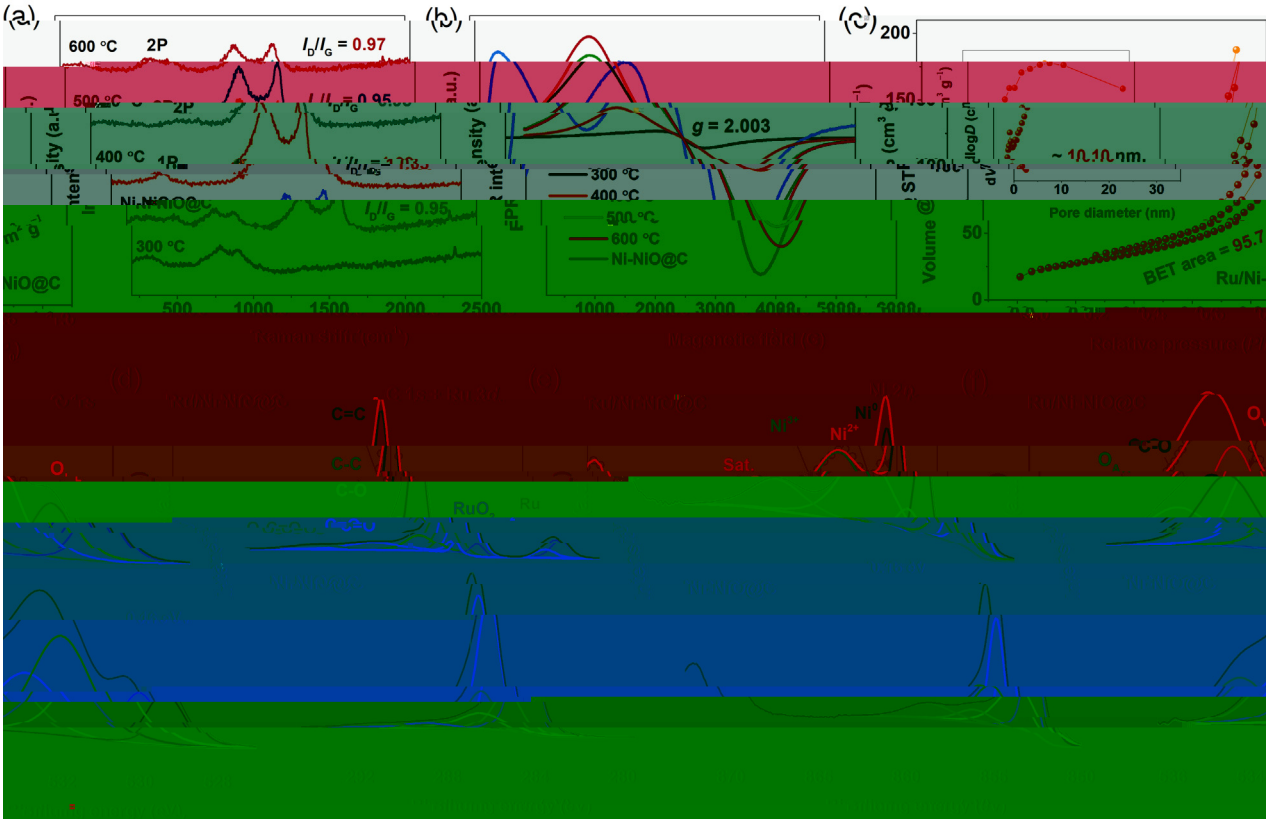

Fig. 2. (a) Raman spectra and (b) EPR spectra of as-synthesized samples at different temperatures. (c) N_2 adsorption/desorption isotherm with the inset showing the corresponding pore size distribution of Ru/Ni-NiO@C. High-resolution XPS spectra of (d) C 1*s* + Ru 3*d*, (e) Ni 2*p*, and (f) O 1*s* regions in Ru/Ni-NiO@C and Ni-NiO@C, respectively.

Ru/NiO@C (300 °C), Ru/Ni-NiO@C-500, and Ru/Ni-NiO@C-600 show two peaks at 770 and 900 cm^{-1}, while the Ru/Ni-NiO@C Raman spectrum shows one peak at 520 cm^{-1}. According to the precedent studies, $1P_{LO}$ mode (at 520 cm^{-1}) is Raman inactive in a perfect single crystal, but surface effect or the presence of vacancy makes it visible [23]. In addition, in-depth studies have revealed that Ni vacancy concentration dominates the intensity of $1P_{LO}$ mode [23,32]. However, when $1P_{LO}$ becomes more pronounced due to the presence of nickel vacancies, two bands of $2P_{TO}$ (770 cm^{-1}) and $2P_{TO+LO}$ (900 cm^{-1}) will be broader and even disappear [33]. The existence of $1P_{LO}$ mode can be attributed to large amounts of innate nickel vacancies in Ru/Ni-NiO@C. Abundant Ni vacancy-induced defects in the interface of Ni-NiO heterostructure can provide more active sites [23]. Oxygen vacancies were well reported as they are the common theme in metal oxides and particularly relevant for promoting catalytic activities [34]. We then resorted to the EPR for direct oxygen vacancies identification (Fig. 2b). The apparent symmetrical signals at g = 2.003 correspond to oxygen vacancies of the samples except for Ru/NiO@C [35]. A monotonic increase in the oxygen vacancy concentration is observed with increasing annealing temperature. Compared with Ni-NiO@C, the EPR intensity of Ru/Ni-NiO@C was attenuated somewhat, which possibly due to the Ru-species effectively occupied some of oxygen defect sites. The vacancies (oxygen-vacancy and nickel-vacancy) introduced in Ru/Ni-NiO@C can substantially modify its electronic properties, leading to its enhanced HOR activity [36]. Analysis of Brunauer-Emmett-Teller (BET) adsorption-desorption isotherm indicates that the specific surface area of Ru/Ni-NiO@C is 95.7 $m^2\ g^{-1}$. Additionally, the pore size distribution of Ru/Ni-NiO@C is 10.10 nm, indicating that it is a mesoporous material. These mesopores act as isolators, which can prevent Ru NPs from stacking and increase the access of active sites (Fig. 2c) [37].

The depth profile XPS elucidated the surface chemical constitution and electron state of the samples. XPS analysis of Ru/Ni-NiO@C confirms the presence of C, O, Ni, and Ru elements (Fig. S1). The deconvoluted high-resolution XPS spectra of C 1*s* + Ru 3*d* regions in Fig. 2(d) display the main sharp and strong peaks at C=C (284.0 eV), C–C (284.8 eV), and C–O (286.1 eV) and used as calibration standard [38]. Meanwhile, the Ru $3d_{5/2}$ core level can be divided into two groups of peaks at 280.0, 283.7 eV (Ru^0 3*d*) and 280.5, 284.5 eV (RuO_2 3*d*), respectively. As shown in Fig. 2(e), the high-resolution Ni 2*p* spectra of Ru/Ni-NiO@C are disassembled into four peaks at 852.4, 853.1, 855.7, and 861.1 eV, which are ascribed to metallic Ni, Ni^{2+}, Ni^{3+}, and satellite peaks, respectively, suggesting the part of Ni^{2+} was successfully reduced to Ni^0 through the carbonization process [23]. XPS analysis also provides the foremost evidence of the coexistence of Ni^{2+} and Ni^{3+}. The presence of Ni^{3+} suggests Ni vacancies are successfully incorporated into the lattice of Ru/Ni-NiO@C during annealing. The oxidation of Ni^{2+} to Ni^{3+} to maintain charge balance of near-surface Ni vacancies echoes the above Raman results [23]. Interestingly, the XPS peak belonging to Ni^0 in Ru/Ni-NiO@C illustrates a positive shift (0.16 eV) compared to Ni-NiO@C, indicating a strong electronic effect between Ni and Ru species [39]. The XPS analysis further demonstrates a strong electronic interaction occurring between Ru and Ni-NiO@C, which Ru could effectively reshape the electronic structure of Ni species. Furthermore, we also examined the oxygen vacancies formation by the O 1*s* core level XPS spectra of Ru/Ni-NiO@C (Fig. 2f). The asymmetric O 1*s* peak can be deconvoluted into four peaks existing at 529.3, 530.7, 531.5, and 532.8 eV, conforming to lattice oxygen (O_L), oxygen vacancies

(O_V), C–O bond, and surface adsorbed oxygen species (O_A), respectively [40]. Clearly, a negative binding energy (BE) shift (ca. 0.16 eV) is observed for O 1*s* in Ni-NiO@C compared with Ru/Ni-NiO@C, indicating that electrons are transferred to the neighboring oxygen vacancies [40]. According to the integrated peak areas, the concentration of oxygen vacancies [$S_{\text{oxygen vacancy}}$/ ($S_{\text{oxygen vacancy}}$ +- $S_{\text{lattice oxygen}}$)] of Ru/Ni-NiO@C (0.69) is lower than Ni-NiO@C (0.76), which is likely that the Ru-species occupied some of defects induced by O vacancies in Ru/Ni-NiO@C. These results match well with EPR analyses. Combining the results mentioned above, it is clear that an active nanostructure is formed with Ru NPs coupled with nickel/oxygen vacancies, which can enhance electronic interaction and accelerate interfacial electron transfer rate between Ru and Ni-NiO@C [41,42].

3.3. SEM and TEM characterizations

The morphological evolution of the Ru/Ni-NiO@C composite was tracked by SEM. As depicted in Fig. 3(a), Ru/Ni-NiO@C shows the typical microspherical hollow morphology preserved from Ni-MOF (Fig. S2), which can furnish large free space for Ru loading. The average diameter of Ru/Ni-NiO@C was estimated to be approximately 1 μm. Notably, the microsphere's surface covered a large quantity of nanoparticles, thus forming a hierarchical order at micro/nano levels, which also well demonstrated the effectiveness of our synthetic strategy toward supported nanoparticles with high homogeneity. Such mirco/nano superstructure favors to provide a large fraction of electrochemical accessible surface area [43]. Further, the hierarchical hollow nature was also confirmed by the TEM image (Fig. 3b), evident from the bright-dark contrast variation between edges and centers. The statistical results of about 200 Ru and Ni-NiO NPs concluded that the average particle size is approximately 1.28 nm for Ru NPs and 9.15 nm for Ni-NiO NPs (Figs. S3 and S4). From the high-resolution TEM (HRTEM) image (Fig. 3c), Ru, Ni, and NiO phases are found on the microspherical surface. The lattice distance of one NP is about 0.18 nm, which can be indexed to (200) plane of cubic Ni. The well-resolved lattice fringes with the inter-planar distance of about 0.21 and 0.16 nm are assigned to NiO (200) plane and metallic Ru (102) plane, respectively. The existence of Ni and NiO in Ru/Ni-NiO@C was further supplemented by the selected area electron diffraction (SAED) pattern (Fig. S5a). The prominent electron diffraction rings or aggregated dots belong to Ni (200) and NiO (200) phases. At the same time, Ru is amorphous, and no evident diffraction ring is observed, consistent with XRD results. Moreover, the HRTEM image also demonstrates several curved graphene layers from the carbon frameworks, which serve as protective shells that contribute to prevention of coalescence of Ru NPs during annealing [44]. The carbon-coated structure is formed during the pyrolysis of MOF. Undoubtedly, this carbon-coated structure can effectively improve the electrical conductivity of the transition metal nanoparticles and protect the active centers from corrosion by alkalis [20,45]. As shown in Fig. 3(d) and Fig. S5(b), the high-angle annular dark-field scanning transmission electron microscopy (HAADF-STEM) image and corresponding elemental mappings of Ru/Ni-NiO@C further corroborate the coexistence of C, O, Ni, and Ru in the entire sample.

3.4. Electrocatalytic HOR in alkaline electrolytes

The HOR electrocatalytic activity of as-prepared catalysts was first probed by using the rotating disk electrode (RDE) technique in H_2-saturated 0.1 M KOH electrolyte. The reversible hydrogen electrode (RHE) calibration was performed before measurements (Fig. S6), and electrochemical data were presented with *iR*-corrected (Fig. S7). Initially, we performed quick screening experiments according to the TGA results, therefore the annealing temperature is fixed at 400 °C to optimize the Ru loading on the catalytic activity of Ru/Ni-NiO@C. As shown in Fig. 4(a), electrocatalytic performance of Ru/Ni-NiO@C varied with the change of Ru loading from 2.9 to 5.1 wt%, in which the sample with 3.8 wt% Ru (denoted as Ru/Ni-NiO@C) loading stands out as the best HOR catalyst among the series, showing that the appropriate Ru loading is vital for successful Ru utilization. Tafel plots in Fig. 4(b) also validate the fastest HOR kinetics on Ru/Ni-NiO@C. Fig. 4(c) reveals that the kinetic current density (j_k) at 50 mV and electrochemical active surface area (ECSA)-normalized exchange current density ($j_{0,s}$) values show parabolic behaviors, where the maximum values of $j_{k\ @\eta\ =\ 50\ mV}$ (32.61 mA cm^{-2}) and $j_{0,s}$ (0.084 mA cm^{-2}) from the micro-polarization region (−10 to 10 mV) by linear fitting through the Butler-Volmer equation (Fig. S8) are obtained with 3.8 wt% Ru loading is chosen as the basis for the subsequent experiments.

The catalyst performance depends on the phase and Ni/NiO ratio of the resultant products governed by the annealing temperature. We utilized XPS analysis to investigate the surface chemical composition of the samples. As shown in Fig. S9(a), Ru/NiO@C (300 °C) does not have metallic Ni in its structure because the carbonization rate is relatively low at 300 °C, which is in line with TGA and XRD results. The Ru/NiO@C (300 °C) sample, featuring only the NiO phase, shows nearly inactive toward HOR, demonstrating the promotional effect of metallic Ni on uplifting the intrinsic activity of HOR (Fig. 4d–f). To verify the pivotal role of the Ni/NiO ratio in the HOR activity, we analyzed Ni/NiO ratio quantitatively in developed catalysts via XPS. An increase of metallic Ni can be observed with the annealing temperature is elevated from 400 to 600 °C (Fig. S9a). The XPS survey spectra demonstrated the coexistence

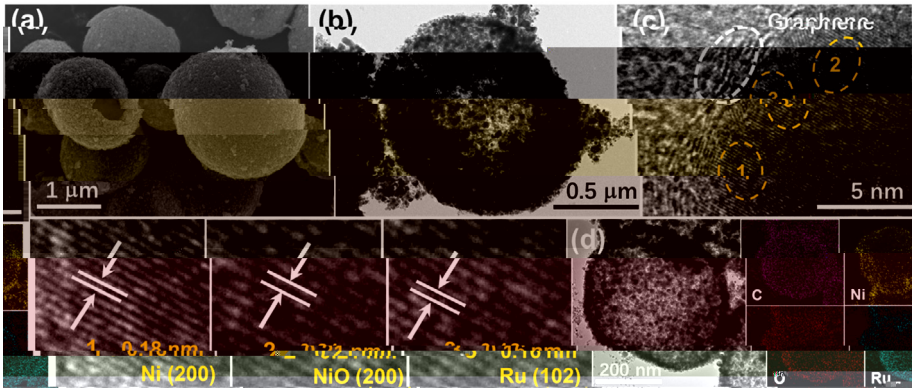

Fig. 3. (a) SEM image, (b) TEM image, (c) high-resolution TEM images, and (d) HAADF-STEM image and corresponding elemental mappings of Ru/Ni-NiO@C.

of the Ni and NiO phase in the samples, and Ni/NiO ratio is quantitatively determined to be 1.6, 2.3, and 3.5 for Ru/Ni-NiO@C-400, Ru/Ni-NiO@C-500, and Ru/Ni-NiO@C-600, respectively (Table S2). Correspondingly, anodic current densities were significantly decreased in the RDE voltammogram with the Ni/NiO ratio increase. The result demonstrates Ru/Ni-NiO@C annealed at 400 °C possesses an optimal Ni/NiO ratio, which is responsible for enhancing HOR. The relationship between Ni/NiO ratio and HOR activity is further visualized in Fig. S10.

The surface vacancies of electrocatalysts may induce positive effects on an electrochemical reaction. We next tried to quantify the nickel/oxygen vacancies in NiO species by XPS to unveil the vacancy-activity relationship. The content ratio was calculated based on the proportion of its fitting peaks [31]. The XPS survey spectra demonstrated the successful introduction of nickel/oxygen vacancies, with a content Ni^{3+} ratio of 82.2%, 59.9%, 62.2%, and 49.1%, while the content ratio of oxygen vacancies is 64.4 %, 68.1%, 70.2 %, and 77.1 % for Ru/NiO@C-300, Ru/Ni-NiO@C-400, Ru/Ni-NiO@C-500, and Ru/Ni-NiO@C-600, respectively (Fig. S9b and Table S2). It can be seen the general decrease in nickel vacancies concentration but an increase in oxygen vacancies concentration with the increase of annealing temperature. Then, we investigated the effect of nickel/oxygen vacancies concentration on the HOR performance. The linear sweep voltammetry (LSV) curves in Fig. 4(d) show that the HOR anodic current density was apparent attenuation when the pyrolysis temperature was increased from 400 to 600 °C. Hence, the ideal performance at 400 °C can be ascribed to the synergistic optimization of both nickel and oxygen vacancies concentration. Besides, the HOR performance parameters of all samples were given in Table S3.

HBE has been considered as a key descriptor to evalulate HOR activity [10,15,46]. The hydrogen under-potential deposition (H_{upd}) peaks in a cyclic voltammogram (CV) directly correlate with HBE. The peak at the lower potential in the H_{upd} region corresponds to the weaker metal–H bond strength. In comparison, the one at higher potential relates to the stronger metal–H bond strength [47], and the weaker HBE is more conducive to HOR [48]. Previous studies demonstratesd that high HOR performance generally depends on two factors. Firstly, because of the stronger electron-transfer interaction, the adsorption capability of small adsorbates (such as CO_{ad} and H_{ad}) on catalysts surface would be weakened, which effectively promotes alkaline HOR performance [15,49]. On the other hand, Xie et al. desinged a new Rh@Pt_x with surface defects, pointing out the importance of structural defects toward HOR activity [50]. In Fig. 5(a), the CV curves of Ru/Ni-NiO@C were tested in N_2-saturated 0.1 M KOH with reference measurements of Ni-NiO@C, Pt/C, and Ru/C for comparison. The H_{upd} peak potential of Ru/Ni-NiO@C (0.17 V vs. RHE) is more negative than that of Pt/C (0.30 V vs. RHE), possibly due to the presence of surface vacancies and weakened HBE [50], reflecting the Ru/Ni-NiO@C possesses the higher HOR activity than Pt/C. In constrast, Ni-NiO@C and benchmark Ru/C show unremarkable H_{upd} peaks, reaveling the strong electronic interaction between Ru and Ni-NiO@C species can weaken the HBE [15,49].

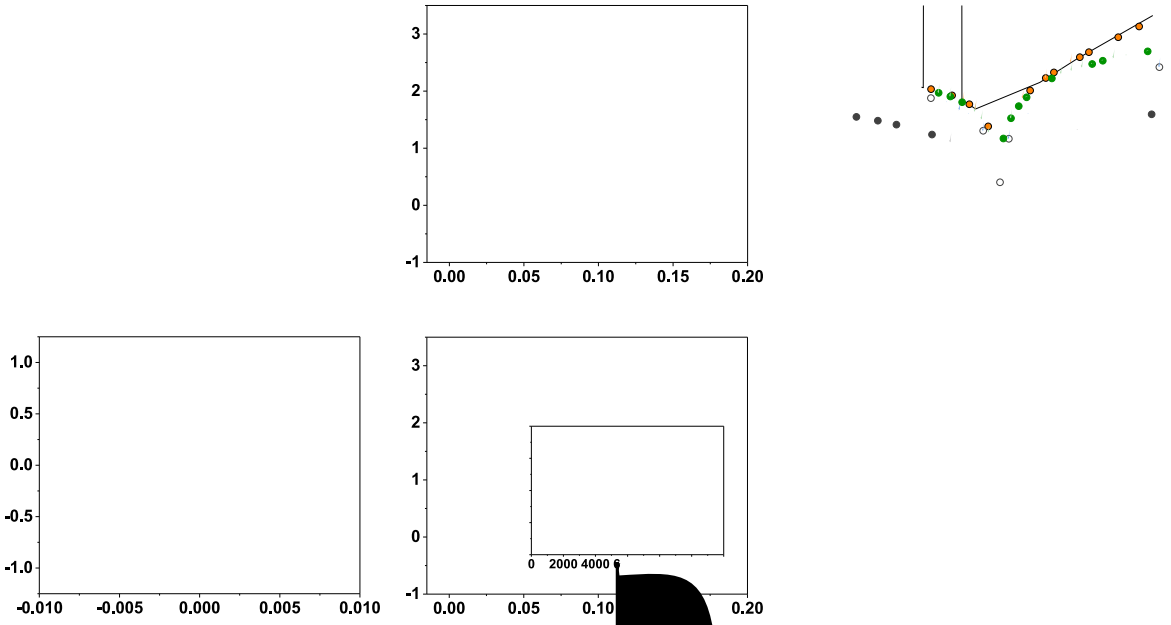

is evaluated from linear fitting of micropolarization regions (−10 to 10 mV), in which the slope is proportional to j_0 [51]. We show the $j_{0,s}$ and find that the $j_{0,s}$ is 0.084 mA cm^{-2} for Ru/Ni-NiO@C, comparable to Pt/C (0.095 mA cm^{-2}) catalyst, impling good intrinsic HOR activity of Ru/Ni-NiO@C (Table S3). Fig. 5(e) shows the polarization curves of Ru/Ni-NiO@C before and after 1000 CV cycles, the two polarization curves almost overlap. Moreover, we also assessed the stability of Ru/Ni-NiO@C by chronoamperometry at η = 50 mV, which delivers a stable current density without degradation throughout the test. As demonstrated in Fig. S15, Ru/Ni-NiO@C-After catalyst still preserves its pristine morphology. Moreover, we find that the Ru/Ni-NiO@C-After still has Ru, Ni^0, Ni^{2+}, Ni^{3+}, and O$_v$ signals, and the peak intensities were similar to Ru/Ni-NiO@C even after the long-term stability test (Fig. S16). In conclusion, these results clearly indicate that our developed catalyst bears a robust surface structure that protects the active centers from alkali corrosion during HOR. Apart from kinetics current and exchange current evaluation of catalysts, the metal loading normalized data comparison gives a more accurate picture of catalyst activity. The mass activity of Ru/Ni-NiO@C is calculated to be 2.79 mA μg_{Ru}^{-1}, exceeding most of the previous electrocatalysts (Fig. 5f and Tables S3 and S4).

As Ru is susceptible to oxidation in the hydrogen adsorption/desorption potential region, it is not suitable to calculate the ECSA by measuring the charge associated with the H_{upd} region. Therefore, we performed CO stripping voltammetry to measure the ECSA value of samples. As shown in Fig. 6, the ECSA of Ru/Ni-NiO@C was estimated to be 52.9 m^2 g^{-1}, higher than Pt/C (48.1 m^2 g^{-1}) and Ru/C (15.8 m^2 g^{-1}). The ECSAs of other catalysts were summarized in Table S3. Higher ECSA implies more active sites for catalytic reactions, which favors the close contact of reactants with electrolyte [52]. The excellent HOR activity of Ru/Ni-NiO@C motivated our investigation for its hydrogen evolution reaction (HER). Ru/Ni-NiO@C shows an excellent HER activity and stability, and is among the best precious metal based electrocatalysts (Figs. S17 and S18 and Table S5).

3 [illegible] *hancement mechanism*

[illegible]atic theories and operando experiments have demonst[illegible]t HBE and OHBE are the descriptors to precisely interp[illegible]nderlying causes of activity enhancement of alkaline H[illegible]]. Considering that OH_{ad} species can accelerate the r[illegible] CO_{ad} species intermediate on metal surface, and the C[illegible]ng potential is correlated directly with the strength of O[illegible]rption adsorption [8,15]. Further, the electronic effect o[illegible] surface structure of Ru/Ni-NiO@C can decrease H_{ad} inter[illegible]binding energy and the adsorption strength of CO_{ad} [49]. T[illegible]-stripping experiments were further conducted to monit[illegible]H binding of the catalysts, and their results were recorded i[illegible]n Fig. 6(a and b), the CO oxidation peak of Ru/Ni-NiO@C is a[illegible]3 V, which can be seen clearly that Ru/Ni-NiO@C exhibits t[illegible]gest OH^- adsorption among these materials [53]. In Fig. 6 ([illegible], the CO oxidation peaks of Pt/C and Ru/C are at 0.74 and 0[illegible]revious studies investigating the sluggish HOR kinetics of P[illegible]uded that its weak OH_{ad} binding in alkaline [8,54]. Our CO st[illegible]g results indicate that enhanced OH_{ad} on Ru/Ni-NiO@C n[illegible]ccount for the enhancement of alkaline HOR performance. A[illegible]aled by the CV behavior, the weakening of H_{ad} binding e[illegible]s due to the incorporation of Ru yields an electronic effect a[illegible]u and Ni-NiO@C interface and surface defects induced by N[illegible]acancies, as XPS showed [15,50,55]. To bring theoretical in[illegible]s into the HOR mechanism of Ru/Ni-NiO@C and pinpoint th[illegible]ive sites, we conducted DFT calculations. Fig. S19 shows th[illegible]imal structure model of Ru/Ni-NiO@C (details in Computati[illegible]methods). The differential charge density of Ru/Ni-NiO@C s[illegible] that there is overt charge depletion around Ni and charge a[illegible]ulation around Ru, again interpreting the strong electronic in[illegible]tion between Ru and Ni species (Fig. 7a). We examined vario[illegible]ossible sites on Ru, Ni, and NiO position in Ru/Ni-NiO@C to c[illegible]te their HBE and OHBE (Figs. S20 and S21). Fig. 7(b) shows th[illegible]timal adsorption sites of H_{ad}, the calculated HBE on Ru sites w[illegible]-0.41 eV, very close to the binding energy on Pt (111) ([illegible]) eV), and eventually results in the theoretical optimal value

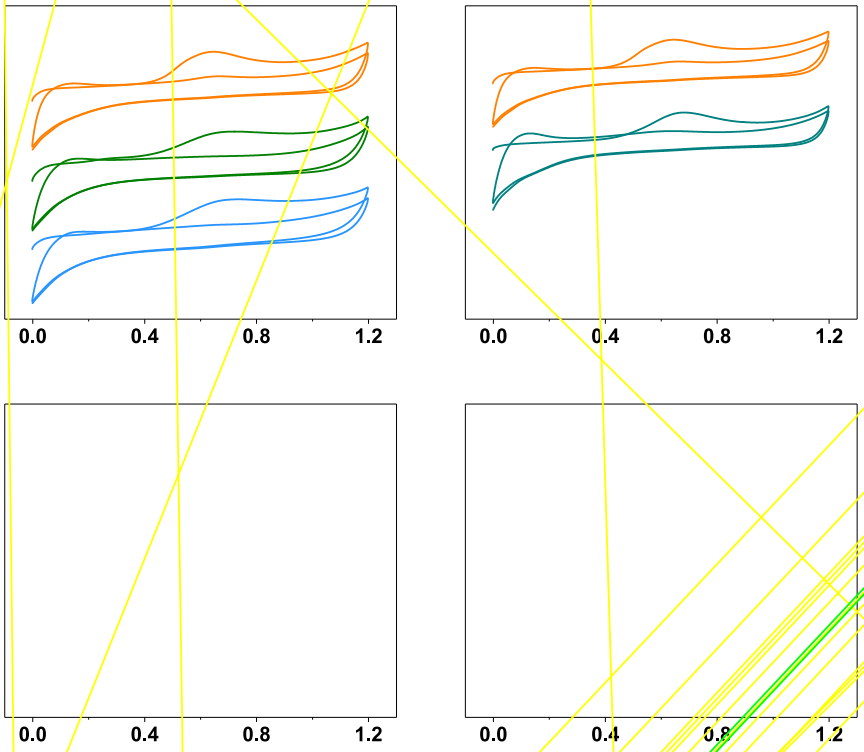
0.0
0.4
0.8
1.2
0.0
0.4
0.8
1.2
0.0
0.4
0.8
1.2
0.0
0.4
0.8
1.2

of ΔG_{H^*} (ΔG_{H^*} = 0 eV) [7]. Therefore, the much-weakened HBE on Ru sites is a synergistic electronic effect between Ru and Ni species, which tremendously facilitates the critical Volmer step, leading to the HOR enhancement [17]. Fig. 7(c) presents optimal OH_{ad} sites on NiO with a binding energy of −0.74 eV, giving a very similar OHBE with Pt(111) (−0.87 eV) model compared with Ru (−0.55 eV) and Ni (−0.59 eV) [7]. Such a strengthened OH_{ad} adsorptive behavior results from the surface structure containing nickel/oxygen vacancies, contributing to capturing OH^* species on the NiO surface [17], thereby promoting the Volmer step during alkaline HOR process and enabling Ru/Ni-NiO to follow the bifunctional mechanism at the Ru and Ni-NiO@C interface, with adsorption of H_{ad} on Ru and OH_{ad} on NiO sites. Besides, Ni arguably plays an auxiliary role in accelerating the charge transport [23]. Thus, a bifunctional mechanism that balanced both optimal HBE and OHBE is proposed for Ru/Ni-NiO@C in alkaline medium, as shown in Fig. 7(d).

Based on the characterizations and experiemtal results, the augmenting HOR activity of Ru/Ni-NiO@C arises from the following aspects: (1) The flexible cavities and hierarchically porous structure favor the mass/charge transportation [56]. (2) Strong electronic interactions between Ru species and Ni-NiO@C support can reduce the interfacial impedance and expedite HOR kinetics [57]. (3) Annealing induces Ni and O vacancies in Ru/Ni-NiO@C to enhance electronic conduction and generate additional catalytically active sites [23,58]. (4) High conductivity of carbon and metal Ni facilitates electron transportation [20,23]. (5) Synergistic interplay of both optimal H_{ad} and OH_{ad} on Ru/Ni-NiO@C surface substantially promotes the key Volmer step [7,49].

4. Conclusions

In summary, we reported a rational manipulation strategy to construct Ru/Ni-NiO@C electrocatalyst via a MOF-engaged replacement-pyrolysis method, in which Ru NPs are coated onto the hollow Ni-NiO@C, forming an intimately contacted superstructure. Utilizing the mutual interaction between metal Ru and vacancies-rich Ni-NiO@C support achieves not only desirable dispersity but also regulated interfaces. Annealing treatment at 400 °C induces vacancies in Ru/Ni-NiO@C, which provides additional insights in the reactivity of the active sites. The vacancies can act as a "claw" to capture and couple firmly with Ru species, thus optimize the charge transfer and catalytic active sites. DFT calculations reveal that electronic interaction between Ru and Ni-NiO@C, together with vacancy-rich NiO species contribute to the optimal HBE and enhanced OHBE, collectively shifting the HOR activity toward the vertex of the volcano plot. Specifically, the HOR mass activity of Ru/Ni-NiO@C is 2.79 mA μg_{Ru}^{-1}, which is 7.75 times higher than that of Pt/C catalyst. The Ru/Ni-NiO@C also shows high durability without degradation over 1000 cycles. This work presents a facile scenario to construct catalytic sites using vacancy defects. It offers a promising approach for cost-effective precious-metal-based catalysts in the field of hydrogen oxidation.

Declaration of competing interest

The authors declare that they have no known competing financial interests or personal relationships that could have appeared to influence the work reported in this paper.

Acknowledgments

This work has been supported by the National Natural Science Foundation of China (21965005), the Natural Science Foundation of Guangxi Province (2018GXNSFAA294077, 2021GXNSFAA076001), the Project of High-Level Talents of Guangxi (F-KA18015), and the Guangxi Technology Base and Talent Subject (GUIKEAD18126001, GUIKE AD20297039).

Appendix A. Supplementary data

Supplementary data to this article can be found online at https://doi.org/10.1016/j.jechem.2022.06.011.

References

[1] J. Zheng, Z. Zhuang, B. Xu, Y. Yan, ACS Catal. 5 (2015) 4449–4455.
[2] G. Zhao, J. Chen, W. Sun, H. Pan, Adv. Funct. Mater. 31 (2021) 2010633.
[3] Y. Xue, L. Shi, X. Liu, J. Fang, X. Wang, B.P. Setzler, W. Zhu, Y. Yan, Z. Zhuang, Nat. Commun. 11 (2020) 5651.
[4] L. Su, D. Gong, Y. Jin, D. Wu, W. Luo, J. Energy Chem. 66 (2022) 107–122.
[5] Z. Zhang, H. Liu, L. Ni, Z.-L. Zhao, H. Li, J. Energy Chem. (2022), https://doi.org/10.1016/j.jechem.2022.04.043.
[6] T. Zhao, D. Xiao, Y. Chen, X. Tang, M. Gong, S. Deng, X. Liu, J. Ma, X. Zhao, D. Wang, J. Energy Chem. 61 (2021) 15–22.
[7] Y. Yang, X. Sun, G. Han, X. Liu, X. Zhang, Y. Sun, M. Zhang, Z. Cao, Y. Sun, Angew. Chem. Int. Ed. 58 (2019) 10644–10649.
[8] Y. Duan, Z.-Y. Yu, L. Yang, L.-R. Zheng, C.-T. Zhang, X.-T. Yang, F.-Y. Gao, X.-L. Zhang, X. Yu, R. Liu, H.-H. Ding, C. Gu, X.-S. Zheng, L. Shi, J. Jiang, J.-F. Zhu, M.-R. Gao, S.-H. Yu, Nat. Commun. 11 (2020) 4789.
[9] W. Sheng, M. Myint, J.G. Chen, Y. Yan, Energy Environ. Sci. 6 (2013) 1509–1512.
[10] L. Fu, Y. Li, N. Yao, F. Yang, G. Cheng, W. Luo, ACS Catal. 10 (2020) 7322–7327.
[11] Y. Qiu, L. Xin, Y. Li, I.T. McCrum, F. Guo, T. Ma, Y. Ren, Q. Liu, L. Zhou, S. Gu, M.J. Janik, W. Li, J. Am. Chem. Soc. 140 (2018) 16580–16588.
[12] Y. Yang, X. Shao, S. Zhou, P. Yan, T.T. Isimjan, X. Yang, ChemSusChem 14 (2021) 2992–3000.
[13] Y. Yang, Q. Dai, L. Shi, Y. Liu, T.T. Isimjan, X. Yang, J. Phys. Chem. Lett. 13 (2022) 2107–2116.
[14] B. Tang, X. Yang, Z. Kang, L. Feng, Appl. Catal. B: Environ. 278 (2020) 119281.
[15] Y. Wang, G. Wang, G. Li, B. Huang, J. Pan, Q. Liu, J. Han, L. Xiao, J. Lu, L. Zhuang, Energy Environ. Sci. 8 (2015) 177–181.
[16] S. Deng, X. Liu, X. Guo, T. Zhao, Y. Lu, J. Cheng, K. Chen, T. Shen, Y. Zhu, D. Wang, J. Energy Chem. 54 (2021) 202–207.
[17] F. Yang, X. Bao, P. Li, X. Wang, G. Cheng, S. Chen, W. Luo, Angew. Chem. Int. Ed. 58 (2019) 14179–14183.
[18] J. Yang, W. Li, D. Wang, Y. Li, Adv. Mater. 32 (2020) 2003300.
[19] F.D. Speck, F.S.M. Ali, M.T.Y. Paul, R.K. Singh, T. Böhm, A. Hofer, O. Kasian, S. Thiele, J. Bachmann, D.R. Dekel, T. Kallio, S. Cherevko, Chem. Mater. 32 (2020) 7716–7724.
[20] F. Zou, Y.-M. Chen, K. Liu, Z. Yu, W. Liang, S.M. Bhaway, M. Gao, Y. Zhu, ACS Nano 10 (2016) 377–386.
[21] L. Yan, Y. Xu, P. Chen, S. Zhang, H. Jiang, L. Yang, Y. Wang, L. Zhang, J. Shen, X. Zhao, L. Wang, Adv. Mater. 32 (2020) 2003313.
[22] L. Yan, H. Jiang, Y. Wang, L. Li, X. Gu, P. Dai, D. Liu, S.-F. Tang, G. Zhao, X. Zhao, K.M. Thomas, Electrochim. Acta 297 (2019) 755–766.
[23] A. Tang, C. Wan, X. Hu, X. Ju, Nano Res. 14 (2021) 4063–4072.
[24] G. Kresse, J. Furthmüller, Comput. Mater. Sci. 6 (1996) 15–50.
[25] G. Kresse, J. Furthmüller, Phys. Rev. B 54 (1996) 11169–11186.
[26] J.P. Perdew, K. Burke, M. Ernzerhof, Phys. Rev. Lett. 77 (1996) 3865–3868.
[27] P.E. Blöchl, Phys. Rev. B 50 (1994) 17953–17979.
[28] S. Zhang, H. Xue, W.-L. Li, J. Sun, N. Guo, T. Song, H. Dong, J. Zhang, X. Ge, W. Zhang, Q. Wang, Small 17 (2021) 2102125.
[29] A. Sunny, K. Balasubramanian, J. Raman Spectrosc. 52 (2021) 833–842.
[30] Z. Li, L. Leng, S. Ji, M. Zhang, H. Liu, J. Gao, J. Zhang, J.H. Horton, Q. Xu, J. Zhu, J. Energy Chem. (2022), https://doi.org/10.1016/j.jechem.2022.05.009.
[31] Y.-C. Yin, R.-X. Deng, D.-R. Yang, Y.-B. Sun, Z.-Q. Li, X.-H. Xia, J. Phys. Chem. Lett. 13 (2022) 4350–4356.
[32] A. Sunny, K. Balasubramanian, J. Phys. Chem. C 124 (2020) 12636–12644.
[33] N. Mironova-Ulmane, A. Kuzmin, I. Steins, J. Grabis, I. Sildos, M. Pärs, J. Phys. Conf. Ser. 93 (2007) 012039.
[34] G. Liu, J. Li, J. Fu, G. Jiang, G. Lui, D. Luo, Y.P. Deng, J. Zhang, Z.P. Cano, A. Yu, D. Su, Z. Bai, L. Yang, Z. Chen, Adv. Mater. 31 (2019) 1806761.
[35] H. Xue, A. Meng, T. Yang, Z. Li, C. Chen, J. Energy Chem. 71 (2022) 639–651.
[36] Y. Cao, Y. Su, L. Xu, X. Yang, Z. Han, R. Cao, G. Li, J. Energy Chem. 71 (2022) 167–173.
[37] L. Gong, H. Zhang, Y. Wang, E. Luo, K. Li, L. Gao, Y. Wang, Z. Wu, Z. Jin, J. Ge, Z. Jiang, C. Liu, W. Xing, Angew. Chem. Int. Ed. 59 (2020) 13923–13928.
[38] S. Dou, C. Hu, L. Shi, W. Zhang, S. Zhou, P. Yan, L. D'Souza, T.T. Isimjan, X. Yang, ChemCatChem 13 (2021) 3628–3635.
[39] Z. Liu, X. Yang, G. Hu, L. Feng, ACS Sustain. Chem. Eng. 8 (2020) 9136–9144.
[40] Y. Yao, Y. Zhu, C. Pan, C. Wang, S. Hu, W. Xiao, X. Chi, Y. Fang, J. Yang, H. Deng, S. Xiao, J. Li, Z. Luo, Y. Guo, J. Am. Chem. Soc. 143 (2021) 8720–8730.
[41] Z. Wei, Z. Zhao, J. Wang, Q. Zhou, C. Zhao, Z. Yao, J. Wang, J. Mater. Chem. A 9 (2021) 10160–10168.
[42] Q. Peng, Q. He, Y. Hu, T.T. Isimjan, R. Hou, X. Yang, J. Energy Chem. 65 (2022) 574–582.
[43] Y. Huang, Q. Gong, X. Song, K. Feng, K. Nie, F. Zhao, Y. Wang, M. Zeng, J. Zhong, Y. Li, ACS Nano 10 (2016) 11337–11343.

[44] T.Y. Yoo, J.M. Yoo, A.K. Sinha, M.S. Bootharaju, E. Jung, H.S. Lee, B.-H. Lee, J. Kim, W.H. Antink, Y.M. Kim, J. Lee, E. Lee, D.W. Lee, S.-P. Cho, S.J. Yoo, Y.-E. Sung, T. Hyeon, J. Am. Chem. Soc. 142 (2020) 14190–14200.
[45] Y. Feng, K. Song, W. Zhang, X. Zhou, S.J. Yoo, J.-G. Kim, S. Qiao, Y. Qi, X. Zou, Z. Chen, T. Qin, N. Yue, Z. Wang, D. Li, W. Zheng, J. Energy Chem. 70 (2022) 211–218.
[46] Z. Zhou, Y. Liu, J. Zhang, H. Pang, G. Zhu, Electrochem. Commun. 121 (2020) 106871.
[47] W. Sheng, Z. Zhuang, M. Gao, J. Zheng, J.G. Chen, Y. Yan, Nat. Commun. 6 (2015) 5848.
[48] J. Wu, Y. Zhou, H. Nie, K. Wei, H. Huang, F. Liao, Y. Liu, M. Shao, Z. Kang, J. Energy Chem. 66 (2022) 61–67.
[49] J. Zhang, X. Qu, L. Shen, G. Li, T. Zhang, J. Zheng, L. Ji, W. Yan, Y. Han, X. Cheng, Y. Jiang, S. Sun, Small 17 (2021) 2006698.
[50] J. Cai, X. Liao, P. Li, Q. Wang, H. Huang, Z. Lyu, J. Lin, S. Xie, Chem. Eng. J. 429 (2022) 132414.
[51] D. Liu, S. Lu, Y. Xue, Z. Guan, J. Fang, W. Zhu, Z. Zhuang, Nano Energy 59 (2019) 26–32.
[52] X. Ji, Y. Lin, J. Zeng, Z. Ren, Z. Lin, Y. Mu, Y. Qiu, J. Yu, Nat. Commun. 12 (2021) 1380.
[53] B. Zhang, G. Zhao, B. Zhang, L. Xia, Y. Jiang, T. Ma, M. Gao, W. Sun, H. Pan, Adv. Mater. 33 (2021) 2105400.
[54] D. Strmcnik, M. Uchimura, C. Wang, R. Subbaraman, N. Danilovic, D. van der Vliet, A.P. Paulikas, V.R. Stamenkovic, N.M. Markovic, Nat. Chem. 5 (2013) 300–306.
[55] B. Qin, H. Yu, X. Gao, D. Yao, X. Sun, W. Song, B. Yi, Z. Shao, J. Mater. Chem. A 6 (2018) 20374–20382.
[56] Z. Gao, G. Fan, M. Liu, L. Yang, F. Li, Appl. Catal. B: Environ. 237 (2018) 649–659.
[57] M. Guo, M. Xu, Y. Qu, C. Hu, P. Yan, T.T. Isimjan, X. Yang, Appl. Catal. B: Environ. 297 (2021) 120415.
[58] T. Zhang, M.-Y. Wu, D.-Y. Yan, J. Mao, H. Liu, W.-B. Hu, X.-W. Du, T. Ling, S.-Z. Qiao, Nano Energy 43 (2018) 103–109.